Chin. Phys. Lett. **39**, 047501 (2022)

Quantum Oscillations in Noncentrosymmetric Weyl Semimetal SmAlSi

Weizheng Cao(曹渭征)[1], Yunlong Su(苏云龙)[1], Qi Wang(王琦)[1,2], Cuiying Pei(裴翠颖)[1], Lingling Gao(高玲玲)[1], Yi Zhao(赵毅)[1], Changhua Li(李昌华)[1], Na Yu(余娜)[1], Jinghui Wang(王靖珲)[1,2*], Zhongkai Liu(柳仲楷)[1,2], Yulin Chen(陈宇林)[1,2,3], Gang Li(李刚)[1,2*], Jun Li(李军)[1,2], and Yanpeng Qi(齐彦鹏)[1,2,4*]

[1]*School of Physical Science and Technology, ShanghaiTech University, Shanghai 201210, China*
[2]*ShanghaiTech Laboratory for Topological Physics, ShanghaiTech University, Shanghai 201210, China*
[3]*Department of Physics, Clarendon Laboratory, University of Oxford, Parks Road, Oxford OX1 3PU, UK*
[4]*Shanghai Key Laboratory of High-resolution Electron Microscopy, ShanghaiTech University, Shanghai 201210, China*

(Received 11 November 2021; accepted 15 February 2022; published online 15 March 2022)

As a new type of quantum state of matter hosting low energy relativistic quasiparticles, Weyl semimetals (WSMs) have attracted significant attention for scientific community and potential quantum device applications. In this study, we present a comprehensive investigation of the structural, magnetic, and transport properties of noncentrosymmetric RAlSi (R = Sm, Ce), which have been predicted to be new magnetic WSM candidates. Both samples exhibit nonsaturated magnetoresistance, with about 900% and 80% for SmAlSi and CeAlSi, respectively, at temperature of 1.8 K and magnetic field of 9 T. The carrier densities of SmAlSi and CeAlSi exhibit remarkable change around magnetic transition temperatures, signifying that the electronic states are sensitive to the magnetic ordering of rare-earth elements. At low temperatures, SmAlSi reveals prominent Shubnikov–de Haas oscillations associated with the nontrivial Berry phase. High-pressure experiments demonstrate that the magnetic order is robust and survival under high pressure. Our results would yield valuable insights into WSM physics and potentials in applications to next-generation spintronic devices in the RAlSi (R = Sm, Ce) family.

DOI: 10.1088/0256-307X/39/4/047501

As a new class of quantum materials, Dirac semimetals and Weyl semimetals (WSMs) have attracted significant research.[1] The Dirac fermion is protected by time-reversal (TR) symmetry and space-inversion (SI) symmetry.[2] Once TR or SI symmetry is broken, the Dirac point splits into two Weyl points connected by the "Fermi arc", one of which starts at the sources (+ chirality), and the other terminates at the drains (− chirality).[3,4] The WSM materials found so far can be divided into two groups. One breaks SI, such as the TaAs-family transition metals and related nonmagnetic materials.[5–7] The other breaks TR in magnetic materials, which have been experimentally confirmed in a handful of materials, such as Mn_3X (X = Sn, Ge), $Co_3Sn_2S_2$, and Co_2MnGa.[8–14] Compared with nonmagnetic ones, magnetic WSMs can exhibit unique quantum transport phenomena, such as the large intrinsic anomalous Hall conductivity originating from nontrivial band topology.[15] In this context, magnetic WSMs are special and may lead to potential applications in spintronics.

Recently, RAlSi (R = La, Ce, Pr) with a noncentrosymmetric structure have been predicted to host various WSM states, and the topological characteristics of Weyl fermions have been detected using angle-resolved photoemission spectroscopy and first-principles calculations.[16–18] This new topological family covers nonmagnetic WSM (R = La) and magnetic WSMs (R = Ce, Pr) depending on the rare-earth elements while keeping the same crystal structure. It also offers remarkable tunability of electronic topology with different magnetic ground states and anisotropic magnetic behaviors by varying rare-earth ions. More importantly, the magnetic members of RAlX present rare examples with breaking the SI and TR symmetries; thus, offering peculiar opportunities to study the interplay between magnetism and Weyl fermions in such an interesting system. Although comprehensive studies on the magnetic RAlX, including PrAlGe, CeAlGe, and NdAlSi, unveiled some very likely signatures of the Weyl states, experimental identification for the existence of Weyl fermions are still insufficient and under debate.[16–31] It definitely needs to be further verified in other RAlX members.

Experimentally, to identify the WSM state, a quantum transport study is an essential approach. In this study, we choose two RAlX members with different magnetic ground states: antiferromagnetic (AFM) SmAlSi and ferromagnetic (FM) CeAlSi. We systematically investigate magnetotransport properties

*Corresponding authors. Email: qiyp@shanghaitech.edu.cn; wangjh2@shanghaitech.edu.cn; ligang@shanghaitech.edu.cn
© 2022 Chinese Physical Society and IOP Publishing Ltd

on high-quality single crystals of noncentrosymmetric WSM SmAlSi and CeAlSi. Both samples exhibit nonsaturated magnetoresistance (MR), about 900% and 80% for SmAlSi and CeAlSi (at 1.8 K, 9 T), respectively. The analysis of Shubnikov–de Haas (SdH) oscillations reveals two fundamental frequencies originating from the Fermi surface (FS) pockets with nontrivial π Berry phases. Our high-pressure experiments demonstrate that the magnetic order is robust until a high pressure, indicating potential applications in the next-generation spintronic devices.

Experimental. The single crystals of RAlSi (R = Sm, Ce) were grown using a self-flux method as described in previous studies.[19,32] High-purity blocks of Sm/Ce, Si, and Al were mixed in the molar ratio of 1 : 1 : 10 and loaded into an alumina crucible. All treatments were performed in an argon-filled glove box, and the crucible was sealed in a quartz tube under a vacuum. The quartz tube was heated up to 1100 ℃ in 24 h with temperature holding for 12 h to ensure the raw material melting. Subsequently, the temperature was slowly cooled down to 750 ℃ at a rate of 2 ℃/h, and excessive Al was removed by a high-speed centrifuge.

The crystal surface morphology and composition were examined using scanning electron microscopy and energy dispersive x-ray (EDX) analysis. The phase and quality examinations of both samples were performed on the Bruker AXS D8 Advance powder crystal x-ray diffractometer with Cu $K_{\alpha 1}$ (λ = 1.54178 Å) at room temperature. Rietveld refinements of the PXRD patterns were performed using the TOPAS code.[33] Magnetotransport measurements were performed on the physical property measurement system. The longitudinal and Hall electrical resistivity were measured using a five-probe method. We choose the strategy of sweeping the magnetic field in one direction. Furthermore, we extract the pure Hall resistivity by the equation $\rho_{yx}(\mu_0 H) = [\rho_{yx}(+\mu_0 H) - \rho_{yx}(-\mu_0 H)]/2$ to remove the longitudinal resistivity contribution due to voltage probe misalignment. The magnetization measurement was conducted on a magnetic property measurement system. High-pressure resistivity measurements were performed in a nonmagnetic diamond anvil cell. A cubic BN/epoxy mixture was used to insulate gaskets, and Pt foil was employed in the electrical leads. Pressure was determined using the ruby luminescence method.[34]

Results and Discussion. Figure 1(a) shows the schematic structure of RAlSi (R = Sm, Ce) crystallized in the tetragonal LaPtSi-type structure with space group $I4_1md$ (No. 109). The structure consists of stacks of rare-earth elements (R), Al, and Si layers, and along the [001] direction, each layer consists of only one type of element. Chemical composition analysis using EDX demonstrated that the one-to-one correspondence between actual and nominal compositions is good [Fig. 1(b)]. Figures 1(c) and 1(d) show the refinement powder XRD patterns of SmAlSi and CeAlSi, respectively. The Bragg reflections can be well refined using the Rietveld method with reliability parameters, demonstrating high-quality RAlSi (R = Sm, Ce) crystallized into the noncentrosymmetric structure. Table 1 summarizes the lattice parameters of RAlSi (R = Sm, Ce) obtained in this work.

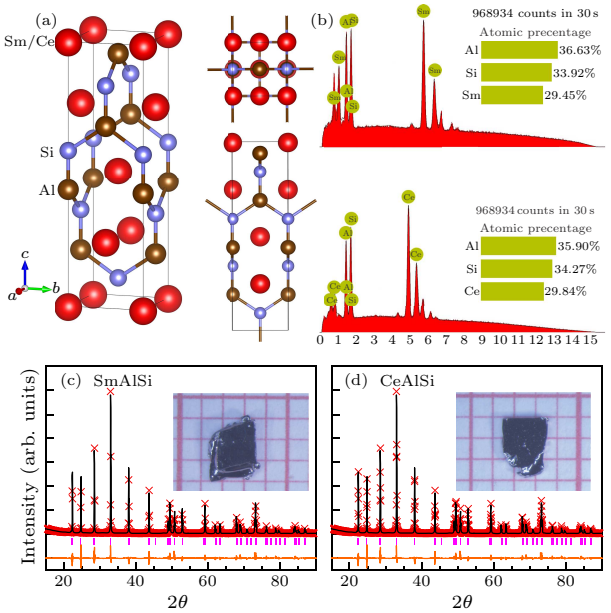

Fig. 1. (a) The crystal structure of RAlSi (R = Sm and Ce). Top and side (as view from a-axis) of RAlSi. (b) Typical EDX spectra of the SmAlSi and CeAlSi single crystals. [(c), (d)] Rietveld refinement of the powder x-ray diffraction patterns of SmAlSi and CeAlSi, respectively. Insets in (c) and (d): The optical images of SmAlSi and CeAlSi, respectively.

Table 1. Structure parameters of RAlSi (R = Sm, Ce).

Compound	SmAlSi	CeAlSi
Space group	$I4_1md$ (No. 109)	
Crystal structure	LaPtSi-type	
a	4.1583 Å	4.2550 Å
c	14.4562 Å	14.5919 Å
V	249.9725 Å^3	264.1857 Å^3
Z	4	4
R_p	4.91%	4.67%
R_{wp}	8.01%	7.32%

Figure 2(a) shows the temperature (T) dependence of longitudinal resistivity (ρ) for SmAlSi. Under zero field, SmAlSi exhibits a typical metallic behavior with residual resistivity of ρ_0 = 17.62 μΩ·cm and residual resistivity ratio RRR = 4.95. As shown in the inset of Fig. 2(a), the resistivity of SmAlSi shows a small anomaly at $T_N \sim 10.7$ K, corresponding to the AFM transition.[35] This magnetic transition was further confirmed by the magnetic susceptibility and isothermal magnetization measurements,

as shown in Figs. 2(b) and 2(c). The effective moment estimated from the Curie–Weiss fit of the magnetic susceptibility above 10 K results in $\mu_{\rm eff} \sim 1.19\mu_{\rm B}$. We also performed the electrical transport and magnetization measurements on high-quality single crystals of CeAlSi. Different from SmAlSi, CeAlSi hosts FM order with Curie temperature ($T_{\rm C}$) of about 9.4 K and effective magnetic moment $\mu_{\rm eff}$ of about 2.54 $\mu_{\rm B}$/Ce.

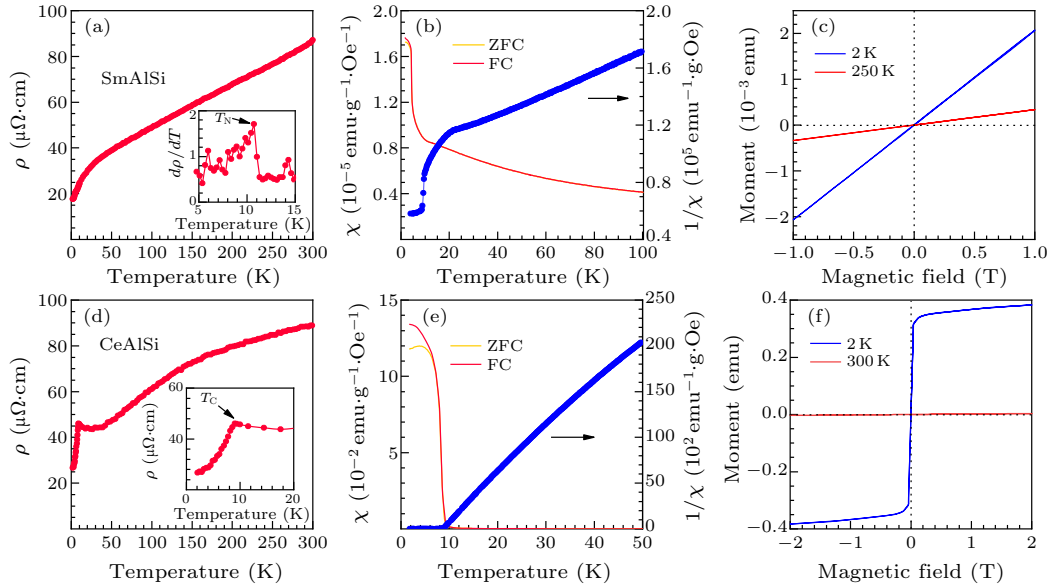

Fig. 2. [(a), (d)] Temperature dependence of resistivity for SmAlSi and CeAlSi in the temperature range from 1.8 K and 300 K. Inset in (a): $d\rho/dT$ of SmAlSi. The $T_{\rm N}$ (about 10.7 K) is taken from the peck of the $d\rho/dT$ curve. Inset in (d): enlarged view of low temperature, showing $T_{\rm C}$ of about 9.4 K. [(b), (e)] Temperature dependence of the in-plane magnetic susceptibility for SmAlSi and CeAlSi, respectively. The inverse of the magnetic susceptibility is also shown. [(c), (f)] Field dependence of the in-plane magnetic moment for SmAlSi and CeAlSi, respectively.

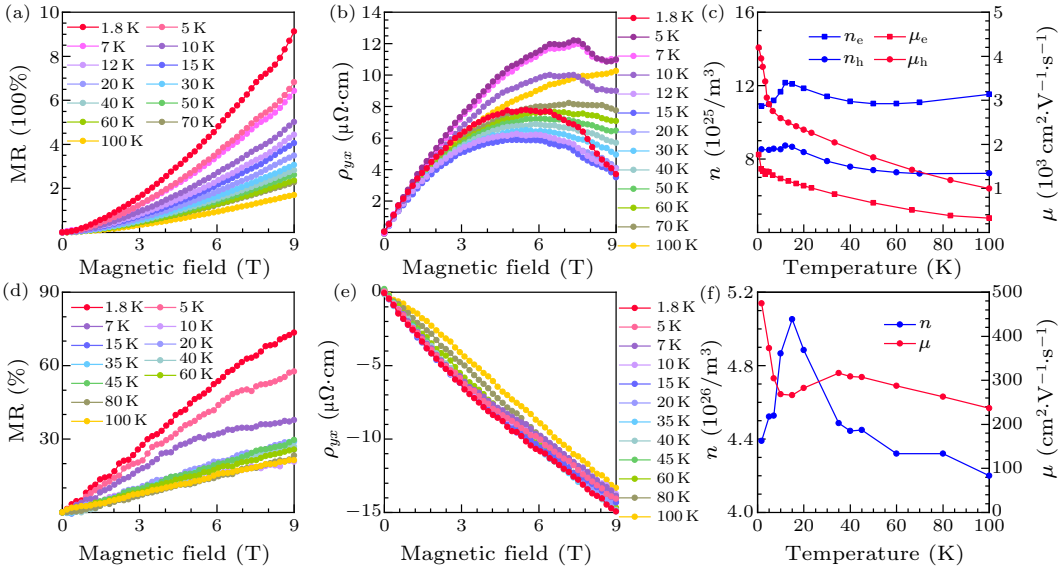

Fig. 3. [(a), (d)] Longitudinal resistivity as a function of magnetic field B at various temperatures for SmAlSi and CeAlSi, respectively. The MR is defined as MR = $[\rho_{xx}(B) - \rho_{xx}(0)]/\rho_{xx}(0) \times 100\%$, where $\rho(B)$ and $\rho(0)$ represent the resistivity with and without B, respectively. [(b), (e)] Hall resistivity for SmAlSi and CeAlSi, respectively. [(c), (f)] Carrier concentration and mobility of SmAlSi and CeAlSi versus temperature, respectively.

Figure 3(a) shows the temperature-dependent MR of SmAlSi, where the magnetic field is along the [001] direction. The MR is defined as MR = $[\rho_{xx}(B) - \rho_{xx}(0)]/\rho_{xx}(0) \times 100\%$, where $\rho_{xx}(B)$ and $\rho_{xx}(0)$ represent the resistivity with and without magnetic field, respectively. At low temperatures, SmAlSi exhibits a large non-saturated MR behavior, and MR reaches about 900% under 9 T at 1.8 K. Figure 3(b) shows the Hall resistivity $\rho_{yx}(B)$ at different temperatures. At 1.8 K, $\rho_{yx}(B)$ shows a nonlinear behavior, and its slope changes sign from positive at low fields to negative at high fields, indicating two types of carriers

coexistent in SmAlSi. To clarify two types of carriers with temperature, we fitted the data using the two-band model:[36]

$$\rho_{xx} = \frac{1}{e}\frac{(n_e\mu_e + n_h\mu_h) + \mu_e\mu_h(n_e\mu_h + n_h\mu_e)B^2}{(n_e\mu_e + n_h\mu_h)^2 + \mu_e^2\mu_h^2(n_h - n_e)^2B^2},$$
$$\rho_{yx} = \frac{B}{e}\frac{(n_h\mu_h^2 - n_e\mu_e^2) + \mu_e^2\mu_h^2(n_h - n_e)B^2}{(n_e\mu_e + n_h\mu_h)^2 + \mu_e^2\mu_h^2(n_h - n_e)^2B^2},$$

where μ_e and μ_h are the mobilities of electrons and holes, respectively; n_e and n_h are the concentrations of electrons and holes, respectively. Figure 3(c) shows carrier concentrations and mobilities as a function of temperature. The carrier densities at 1.8 K reach $n_e = 10.88 \times 10^{25}\,\mathrm{m}^{-3}$ and $n_h = 8.53 \times 10^{25}\,\mathrm{m}^{-3}$ with carrier mobilities $\mu_e = 1.76 \times 10^3\,\mathrm{cm}^2\cdot\mathrm{V}^{-1}\cdot\mathrm{s}^{-1}$ and $\mu_h = 4.20 \times 10^3\,\mathrm{cm}^2\cdot\mathrm{V}^{-1}\cdot\mathrm{s}^{-1}$, which are comparable with other topological semimetals. It is worth noting that the carrier densities (n_e and n_h) display a kink around T_N, indicating that the electronic states are sensitive to the magnetic ordering of Sm moments.

Since the MR of SmAlSi at 1.8 K and 9 T only displays very weak quantum oscillation that is difficult for further analysis, the magnetotransport measurements were then subjected to lower temperature and higher magnetic field. Figure 4(a) shows the resistivity dependence of magnetic field at various temperatures with the magnetic field of about 14 T. Striking SdH quantum oscillations in MR are visible. After subtracting the smooth background, the SdH oscillations at different temperatures from 0.5 K to 20 K against the reciprocal magnetic field $1/B$ are shown in Fig. 4(b). The oscillation patterns show obviously multi-frequency behavior. Furthermore, two fundamental frequencies $F_\alpha = 11.8$ T and $F_\beta = 35.3$ T with their harmonic frequencies $F_{2\beta} = 70.5$ T are identified from the fast Fourier transform analysis (FFT) of SdH oscillations, indicating the presence of at least two FS pockets at the Fermi level [Fig. 4(c)]. According to the Onsager relation $F = (\phi_0/2\pi^2)A_F = (\hbar/2\pi e)A_F$, the cross-sectional areas of the FS normal to the field are $A_\alpha = 1.1 \times 10^{-3}\,\text{Å}^{-2}$ and $A_\beta = 3.4 \times 10^{-3}\,\text{Å}^{-2}$. The values of A_F are comparable with the previous report.[31]

Table 2. Parameters extracted from SdH oscillation for SmAlSi. It is obvious that the yielded Berry phases ϕ_B are $(1.07 \pm 0.25)\pi$ for F_α, and $(1.32 \pm 0.25)\pi$ for F_β. Both Fermi pockets exhibit nontrivial Berry phases.

F (T)	A_F (10^{-3} Å^{-2})	k_F (10^{-2} Å^{-1})	m^* (m_0)	v_F (10^5 m·s^{-1})	E_F (meV)	T_D (K)	τ_D (10^{-13} s)	ϕ_B	μ (cm^2·V^{-1}·s^{-1})
11.8	1.1	1.9	0.1	2.2	27.5	7.9	1.54	$(1.07 \pm 0.25)\,\pi$	0.27
35.3	3.4	3.3	0.09	4.2	90.2	19.2	0.63	$(1.32 \pm 0.25)\,\pi$	0.12

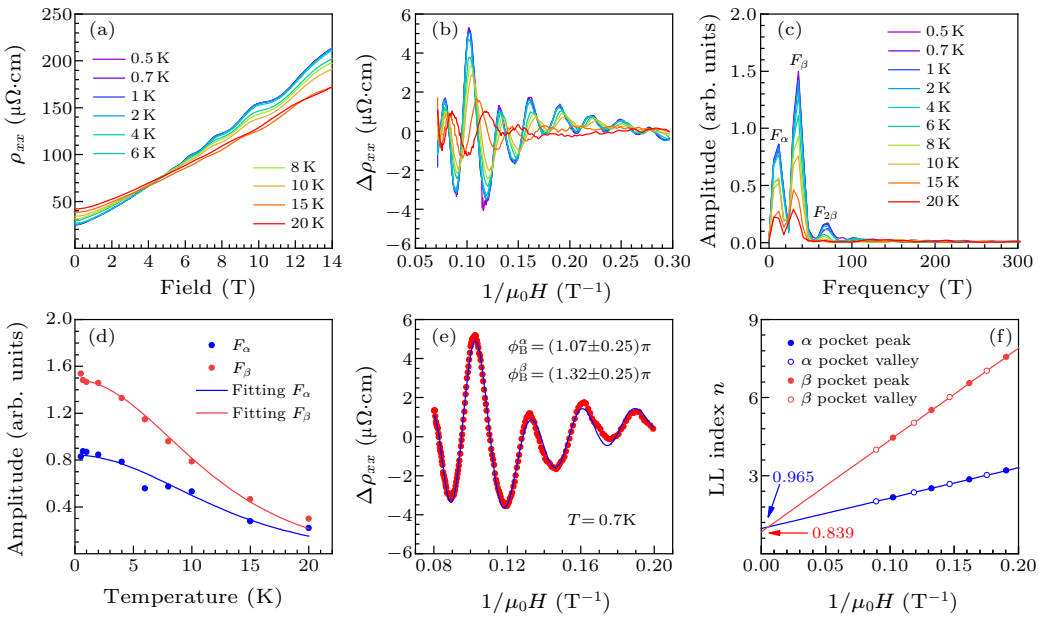

Fig. 4. (a) Magnetic field dependence of resistivity for SmAlSi at various temperatures with the magnetic field along the c-axis. (b) Oscillation patterns $\Delta\rho_{xx} = \rho_{xx} - \langle\rho_{xx}\rangle$ as a function of $1/\mu_0 H$ at various temperatures. (c) FFT spectra of $\Delta\rho_{xx}$ at different temperatures. Two major frequencies of $F_\alpha = 11.8$ T and $F_\beta = 35.3$ T with their harmonic frequencies $F_{2\beta} = 70.5$ T are extracted. (d) The temperature dependence of the FFT amplitudes for major frequencies. The solid lines represent the fits based on the LK formula. (e) The LK fits (blue lines) of SdH oscillations at 0.7 K. (f) Landau level (LL) fan diagram for F_α and F_β at 0.7 K. The solid lines represent the linear fits to the experimental data. The values of the intercepts of the fitting lines with the LL index axis are also shown.

The Dirac/Weyl system will produce a nontrivial ϕ_B under a magnetic field, which could be probed using the Landau level (LL) index fan diagram or a direct fit to the SdH oscillations using the Lifshitz–Kosevich (LK) formula. To gain insight into the topological states of SmAlSi, we perform the analysis of quantum SdH oscillations using the LK formula:[37–39]

$$\Delta\rho^{i}_{xx} \propto \frac{5}{2}\sqrt{\frac{B}{2F}}R_T R_D R_S \cos\left[2\pi\left(\frac{B}{F}+\gamma-\delta+\varphi\right)\right],$$

with $R_D = \exp(-\lambda\mu T_D/B)$, $R_S = \cos(\pi\mu g^*)$, $R_T = \lambda\mu T/[B\sinh(\lambda\mu T/B)]$. Here, $\mu = m^*/m_0$ is the ratio of effective cyclotron mass m^* to free electron mass m_0; T_D is the Dingle temperature; g^* is the effective g factor; $\lambda = 2\pi^2 k_B m_0/e\hbar \approx 14.7\,\mathrm{T/K}$.[40] The oscillatory components of $\Delta\rho$ are expressed by the cosine term with a phase factor $\gamma - \delta + \varphi$, where $\gamma = 0.5 - \phi_B/2\pi$, ϕ_B is the Berry phase. As shown in Fig. 4(d), the small effective cyclotron mass m^* at E_F could be obtained by fitting the temperature dependence of the FFT magnitude to the temperature-damping factor R_T, giving $m^*_\alpha = 0.10m_0$ and $m^*_\beta = 0.09m_0$.[41–43] Additionally, the obtained Dingle temperatures T_D for F_α and F_β are 7.9 K and 19.2 K, respectively. As shown in Fig. 4(e), the LK formula reproduces the resistivity oscillations well at 0.7 K. Taking $\delta = \pm 1/8$ for the three-dimensional system and $\phi = 1/2$ for $\rho_{xx} \gg \rho_{xy}$, the yielded Berry phases ϕ_B are $(1.07 \pm 0.25)\pi$ for F_α, and $(1.32 \pm 0.25)\pi$ for F_β, respectively. Both Fermi pockets exhibit nontrivial Berry phases.[44–46] The results are summarized in Table 2. Figure 4(f) shows the LL fan diagram. All points almost fall on a straight line; thus, allowing a linear fit that gives an intercept of about 0.965 and 0.839 for α and β pocket, respectively. This further demonstrates the nontrivial topological states in SmAlSi.

Furthermore, we performed first-principle calculations using the density-functional theory to understand the electronic structure and magnetic ground states of SmAlSi. All *ab initio* calculations were performed using the full-potential (linearized) (L) augmented plane-wave (APW) + local orbitals (lo) method, as implemented in the Wien2k Package.[47] The exchange-correlation was included by the Perdew–Burke–Ernzerhof.[48] An effective Hubbard energy of 6.4 eV was used to account for the Sm f electrons. Self-consistent calculations throughout the Brillouin zone were conducted with 500 k-mesh. Other values were taken as defaults. We used the open core method to calculate the nonmagnetic electronic structure, as shown in Fig. 5(a). Furthermore, we compared the total energies of the FM and AFM configurations constructed with the primitive cell to examine the magnetic ground states. Consequently, we obtained that the AFM state exhibits lower energy. The calculated local magnetic moment is $5.57\mu_B$/Sm, which is consistent with the six unpaired Sm f electrons; while it is significantly larger than the experimental estimation. This high-spin state in our calculations is the lowest energy state. A low-spin state with roughly $1\mu_B$/Sm seems consistent with experimental estimation. However, it exhibits much higher total energy than the high-spin state, and it is only stable in the FM configuration. The AFM nature is consistent with the experimental measurement on magnetic susceptibility in Fig. 2. Figure 5 shows the electronic structure of the three different magnetic configurations. The solid and dashed lines denote the spin minority and majority components, respectively. Although the presence of local magnetic moments breaks TR and results in the band splitting, the overall electronic structure in AFM states largely resembles that of the nonmagnetic state, which requires further experimental verification.

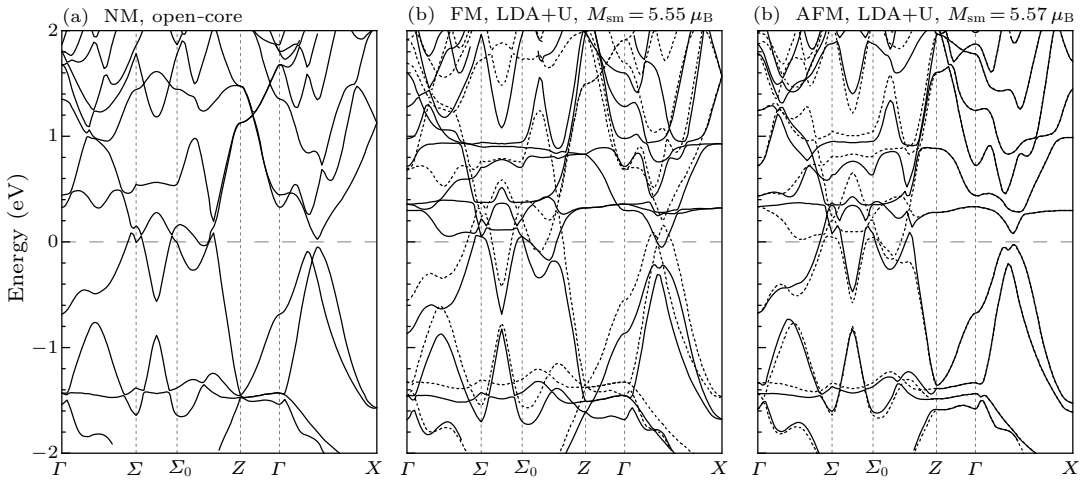

Fig. 5. Electronic structure of SmAlSi in the (a) nonmagnetic, (b) ferromagnetic, and (c) antiferromagnetic states

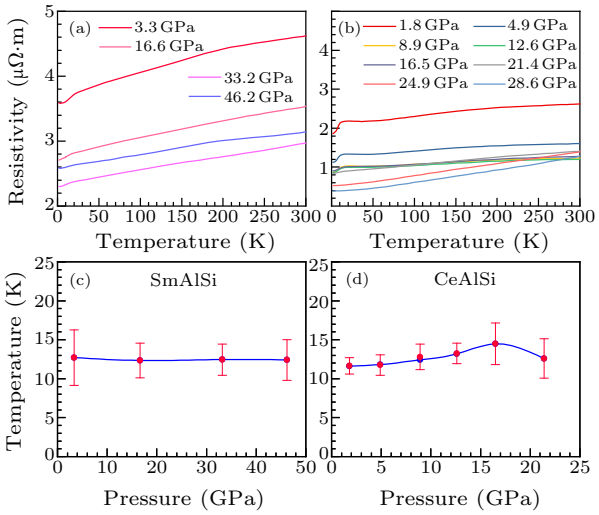

Fig. 6. [(a), (b)] Temperature dependence of electrical resistivity at various pressures for SmAlSi and CeAlSi, respectively. [(c), (d)] Pressure dependence of magnetic transition temperature for SmAlSi and CeAlSi, respectively.

We also performed magnetotransport measurements for CeAlSi. Figures 3(d) and 3(e) show the MR and ρ_{yx} of CeAlSi as a function of the magnetic field with B along the [001] direction, respectively. MR increases with the magnetic field without the trend of saturation. The magnitude of Hall resistivity ρ_{yx} increases down to 100 K. Meanwhile, the Loop Hall effect is observed as shown in Fig. S1 in the Supplemental Information), which is similar to the results reported previously.[32,49] Since CeAlSi is a typical FM with T_C of about 9.4 K, a small AHE is observed. The Hall resistivity ρ_{yx} in an FM traditionally exhibits two parts:[50,51]

$$\rho_{yx} = \rho_{yx}^0 + \rho_{yx}^A = R_0 B + 4\pi R_s M,$$

where ρ_{yx}^0 is the ordinary Hall resistivity; ρ_{yx}^A is the anomalous Hall resistivity; R_0 and R_s represent the ordinary and anomalous Hall coefficients, respectively. Here, ρ_{yx} exhibits almost linear behavior below 100 K. We obtain R_0 by fitting the data at the magnetic field range of 6–9 T, where R_0 demonstrates the negative value, indicating the major role of electron-type carriers for the transport. The electron carrier concentration and mobility temperature dependence were obtained, and the results are shown in Fig. 3(f). It is worth noting that the electron carriers display a kink around T_C, indicating that the electronic states are sensitive to the magnetic ordering of Ce moments. Unfortunately, the low-field MR of CeAlSi displays no quantum oscillations. Thus, the magnetotransport measurements are required to be subject to a high magnetic field.

Both samples exhibit magnetic ground states at low temperature and ambient pressure. Then, we investigate the effect of pressure on the magnetic properties for RAlSi (R = Sm, Ce). Figures 5(a) and 5(b) show the plots of temperature versus resistivity under various pressures for SmAlSi and CeAlSi, respectively. Both samples show a metallic behavior in the entire pressure range. Application of pressure exhibits a weak effect on the magnetic ground state for SmAlSi and CeAlSi. As shown in Figs. 5(c) and 5(d), the Néel temperature T_N and Weiss temperature T_C survive up to 46.2 and 21.4 GPa for SmAlSi and CeAlSi, respectively. The electronic bands exhibit a negligible pressure effect, resulting in a constant magnetic order under high pressure.[49] No superconductivity was observed down to 1.8 K in this pressure range.[52,53] The magnetic WSM RAlSi (R = Sm, Ce) with the nontrivial topology of electronic states display robust magnetic ground states upon compression, which may exhibit potential applications in next-generation spintronic devices.

In summary, we have synthesized high-quality single crystals and performed comprehensive magnetotransport studies on magnetic WSM RAlSi (R = Sm, Ce). Both samples exhibit nonsaturated MR and robust magnetic order, even under high pressure. The analysis of SdH oscillations of SmAlSi reveals two fundamental frequencies originating from the FS pockets with nontrivial π Berry phases. Considering the SI and TR symmetries breaking, our results call for further experimental and theoretical studies on the RAlSi family and related materials to better understand the interplay between magnetic and topological nature and their potential applications in realizing spintronic devices.

Acknowledgment. This work was supported by the National Key R&D Program of China (Grant Nos. 2018YFA0704300 and 2017YFB0503302), the National Natural Science Foundation of China (Grant Nos. U1932217, 11974246, 12004252, 61771234, and 12004251), the Natural Science Foundation of Shanghai (Grant Nos. 19ZR1477300 and 20ZR1436100), the Science and Technology Commission of Shanghai Municipality (Grant Nos. 19JC1413900 and YDZX20203100001438), the Shanghai Science and Technology Plan (Grant No. 21DZ2260400), the Shanghai Sailing Program (Grant No. 21YF1429200), the Interdisciplinary Program of Wuhan National High Magnetic Field Center (Grant No. WHMFC202124), and the Beijing National Laboratory for Condensed Matter Physics. The authors thank the support from Analytical Instrumentation Center (Grant No. SPST-AIC10112914) and Centre for High-resolution Electron Microscopy (C$\hbar$EM) (Grant No. EM02161943), SPST, ShanghaiTech University.

References

[1] Yan B and Felser C 2017 *Annu. Rev. Condens. Matter*

Phys. **8** 337
[2] Liu Z K, Zhou B, Zhang Y, Wang Z J, Weng H M, Prabhakaran D, Mo S K, Shen Z X, Fang Z, Dai X, Hussain Z and Chen Y L 2014 *Science* **343** 864
[3] Wan X, Turner A M, Vishwanath A and Savrasov S Y 2011 *Phys. Rev. B* **83** 205101
[4] Xu S Y, Liu C, Kushwaha S K, Sankar R, Krizan J W, Belopolski I, Neupane M, Bian G, Alidoust N, Chang T R, Jeng H T, Huang C Y, Tsai W F, Lin H, Shibayev P P, Chou F C, Cava R J and Hasan M Z 2015 *Science* **347** 294
[5] Lv B, Weng H, Fu B, Wang X P, Miao H, Ma J, Richard P, Huang X, Zhao L, Chen G, Fang Z, Dai X, Qian T and Ding H 2015 *Phys. Rev. X* **5** 031013
[6] Huang X, Zhao L, Long Y, Wang P, Chen D, Yang Z, Liang H, Xue M, Weng H, Fang Z, Dai X and Chen G 2015 *Phys. Rev. X* **5** 031023
[7] Huang S M, Xu S Y, Belopolski I, Lee C C, Chang G, Wang B, Alidoust N, Bian G, Neupane M, Zhang C, Jia S, Bansil A, Lin H and Hasan M Z 2015 *Nat. Commun.* **6** 7373
[8] Yang H, Sun Y, Zhang Y, Shi W J, Parkin S S and Yan B 2017 *New J. Phys.* **19** 015008
[9] Li X, Xu L, Ding L, Wang J, Shen M, Lu X, Zhu Z and Behnia K 2017 *Phys. Rev. Lett.* **119** 056601
[10] Morali N, Batabyal R, Nag P K, Liu E, Xu Q, Sun Y, Yan B, Felser C, Avraham N and Beidenkopf H 2019 *Science* **365** 1286
[11] Kuroda K, Tomita T, Suzuki M T, Bareille C, Nugroho A A, Goswami P, Ochi M, Ikhlas M, Nakayama M, Akebi S, Noguchi R, Ishii R, Inami N, Ono K, Kumigashira H, Varykhalov A, Muro T, Koretsune T, Arita R, Shin S, Kondo T and Nakatsuji S 2017 *Nat. Mater.* **16** 1090
[12] Belopolski I, Manna K, Sanchez D S, Chang G, Ernst B, Yin J, Zhang S S, Cochran T, Shumiya N, Zheng H, Singh B, Bian G, Multer D, Litskevich M, Zhou X, Huang S M, Wang B, Chang T R, Xu S Y, Bansil A, Felser C, Lin H and Hasan M Z 2019 *Science* **365** 1278
[13] Wang Q, Xu Y, Lou R, Liu Z, Li M, Huang Y, Shen D, Weng H, Wang S and Lei H 2018 *Nat. Commun.* **9** 3681
[14] Liu D F, Liang A J, Liu E K, Xu Q N, Li Y W, Chen C, Pei D, Shi W J, Mo S K and Dudin P 2019 *Science* **365** 1282
[15] Nakatsuji S, Kiyohara N and Higo T 2015 *Nature* **527** 212
[16] Xu S Y, Alidoust N, Chang G, Lu H, Singh B, Belopolski I, Sanchez D S, Zhang X, Bian G and Zheng H 2017 *Sci. Adv.* **3** e1603266
[17] Sanchez D S, Chang G, Belopolski I, Lu H, Yin J X, Alidoust N, Xu X, Cochran T A, Zhang X and Bian Y 2020 *Nat. Commun.* **11** 3356
[18] Chang G, Singh B, Xu S Y, Bian G, Huang S M, Hsu C H, Belopolski I, Alidoust N, Sanchez D S and Zheng H 2018 *Phys. Rev. B* **97** 041104
[19] Zhang K, Wang T, Pang X, Han F, Shang S L, Hung N T, Liu Z K, Li M, Saito R, Huang S 2020 *Phys. Rev. B* **102** 235162
[20] Ng T, Luo Y, Yuan J, Wu Y, Yang H and Shen L 2021 *Phys. Rev. B* **104** 014412
[21] Guloy A M and Corbett J D 1991 *Inorg. Chem.* **30** 4789
[22] Hu Z, Du Q, Liu Y, Graf D and Petrovic C 2020 *Appl. Phys. Lett.* **117** 222410
[23] Hodovanets H, Eckberg C J, Zavalij P Y, Kim H, Lin W C, Zic M, Campbell D J, Higgins J S and Paglione J 2018 *Phys. Rev. B* **98** 245132
[24] Puphal P, Pomjakushin V, Kanazawa N, Ukleev V, Gawryluk D J, Ma J, Naamneh M, Plumb N C, Keller L, Cubitt R, Pomjakushina E and White J S 2020 *Phys. Rev. Lett.* **124** 017202
[25] Meng B, Wu H, Qiu Y, Wang C, Liu Y, Xia Z, Yuan S, Chang H and Tian Z 2019 *APL Mater.* **7** 051110
[26] Destraz D, Das L, Tsirkin S S, Xu Y, Neupert T, Chang J, Schilling A, Grushin A G, Kohlbrecher J, Keller L, Puphal P, Pomjakushina E and White J S 2020 *npj Quantum Mater.* **5** 5
[27] Liu W, Zhao J, Meng F, Rahman A, Qin Y, Fan J, Pi L, Tian Z, Du H, Zhang L and Zhang Y 2021 *Phys. Rev. B* **103** 214401
[28] Lyu M, Xiang J, Mi Z, Zhao H, Wang Z, Liu E, Chen G, Ren Z, Li G and Sun P 2020 *Phys. Rev. B* **102** 085143
[29] Lyu M, Wang Z, Kumar K R, Zhao H, Xiang J and Sun P 2020 *J. Appl. Phys.* **127** 193903
[30] Gaudet J, Yang H Y, Baidya S, Lu B, Xu G, Zhao Y, Rodriguez-Rivera J A, Hoffmann C M, Graf D E, Torchinsky D H, Vanderbilt P N D, Tafti F and Broholm C L 2021 *Nat. Mater.* **20** 1650
[31] Xu L, Niu H, Bai Y, Zhu H, Yuan S, He X, Yang Y, Xia Z, Zhao L and Tian Z 2021 arXiv:2107.11957 [cond-mat.mtrl-sci]
[32] Yang H Y, Singh B, Gaudet J, Lu B, Huang C Y, Chiu W C, Huang S M, Wang B, Bahrami F and Xu B 2021 *Phys. Rev. B* **103** 115143
[33] TOPAS 2013 Version 5 (Karlsruhe, Germany: Bruker AXS)
[34] Mao H K, Xu J A and Bell P M 1986 *J. Geophys. Res.* **91** 4673
[35] Pei C, Xia Y, Wu J, Zhao Y, Gao L, Ying T, Gao B, Li N, Yang W, Zhang D, Gou H, Chen Y, Hosono H, Li G and Qi Y 2020 *Chin. Phys. Lett.* **37** 066401
[36] Ziman J M 2001 *Electrons and Phonons: The Theory of Transport Phenomena in Solids* (Oxford: Oxford University Press)
[37] Shoenberg D 1984 *Magnetic Oscillations in Metals* (Cambridge: Cambridge University Press)
[38] Guo L, Chen T W, Chen C, Chen L, Zhang Y, Gao G Y, Yang J, Li X G, Zhao W Y, Dong S and Zheng R K 2019 *ACS Appl. Electron. Mater.* **1** 869
[39] Xiang F X, Wang X L, Veldhorst M, Dou S X and Fuhrer M S 2015 *Phys. Rev. B* **92** 035123
[40] Ding L, Koo J, Yi C, Xu L, Zuo H, Yang M, Shi Y, Yan B, Behnia K and Zhu Z 2021 *J. Phys. D* **54** 454003
[41] Wang Y Y, Xu S, Sun L L and Xia T L 2018 *Phys. Rev. Mater.* **2** 021201
[42] An L, Zhu X, Qian Y, Xi C, Ning W, Weng H and Tian M 2020 *Phys. Rev. B* **101** 205109
[43] Chen Y, Chen Y, Ning J, Chen L, Zhuang W, He L, Zhang R, Xu Y and Wang X 2020 *Chin. Phys. Lett.* **37** 017104
[44] Luo Y, Ghimire N J, Wartenbe M, Choi H, Neupane M, McDonald R D, Bauer E D, Zhu J, Thompson J D and Ronning F 2015 *Phys. Rev. B* **92** 205134
[45] Luo Y, Ghimire N, Bauer E, Thompson J and Ronning F 2016 *J. Phys.: Condens. Matter* **28** 055502
[46] Zhang K, Du Y, Wang P, Wei L, Li L, Zhang Q, Qin W, Lin Z, Cheng B, Wang Y, Xu H, Fan X, Sun Z, Wan X and Zeng C 2020 *Chin. Phys. Lett.* **37** 090301
[47] Kresse G and Joubert D 1999 *Phys. Rev. B* **59** 1758
[48] Perdew J P, Burke K and Ernzerhof M 1996 *Phys. Rev. Lett.* **77** 3865
[49] Piva M, Souza J, Brousseau-Couture V, Pakuszewski K, John J K, Adriano C, Pagliuso M C P and Nicklas M 2021 arXiv:2111.05742 [cond-mat.mtrl-sci]
[50] Nagaosa N, Sinova J, Onoda S, MacDonald A H and Ong N P 2010 *Rev. Mod. Phys.* **82** 1539
[51] Gao L, Shen S, Wang Q, Shi W, Zhao Y, Li C, Cao W, Pei C, Ge J Y, Li G, Li J, Chen Y, Yan S and Qi Y 2021 *Appl. Phys. Lett.* **119** 092405
[52] Qi Y, Guo J, Lei H, Xiao Z, Kamiya T and Hosono H 2014 *Phys. Rev. B* **89** 024517
[53] Cao W, Zhao N, Pei C, Wang Q, Zhao Y, Gao L, Li C, Yu N, Chen Y, Liu K and Qi Y 2021 arXiv:2111.02882 [cond-mat.supr-con]

Supplemental Information for

Quantum oscillations in Noncentrosymmetric Weyl semimetal SmAlSi

Weizheng Cao(曹渭征)[1], Yunlong Su (苏云龙)[1], Qi Wang(王琦)[1,2], Cuiying Pei(裴翠颖)[1], Lingling Gao (高玲玲)[1], Yi Zhao(赵毅)[1], Changhua Li (李昌华)[1], Na Yu(余娜)[1], Jinghui Wang(王靖珲)[1,2**], Zhongkai Liu(柳仲楷)[1,2], Yulin Chen(陈宇林)[1,2,3], Gang Li(李刚)[1,2**], Jun Li (李军)[1,2], and Yanpeng Qi(齐彦鹏)[1,2,4**]

[1]School of Physical Science and Technology, ShanghaiTech University, Shanghai 201210, China
[2]ShanghaiTech Laboratory for Topological Physics, ShanghaiTech University, Shanghai 201210, China
[3]Department of Physics, Clarendon Laboratory, University of Oxford, Parks Road, Oxford OX1 3PU, UK
[4]Shanghai Key Laboratory of High-resolution Electron Microscopy, ShanghaiTech University, Shanghai 201210, China

**Corresponding authors. Y.Q. (qiyp@shanghaitech.edu.cn); J.W. (wangjh2@shanghaitech.edu.cn) or G. L. (ligang@shanghaitech.edu.cn)

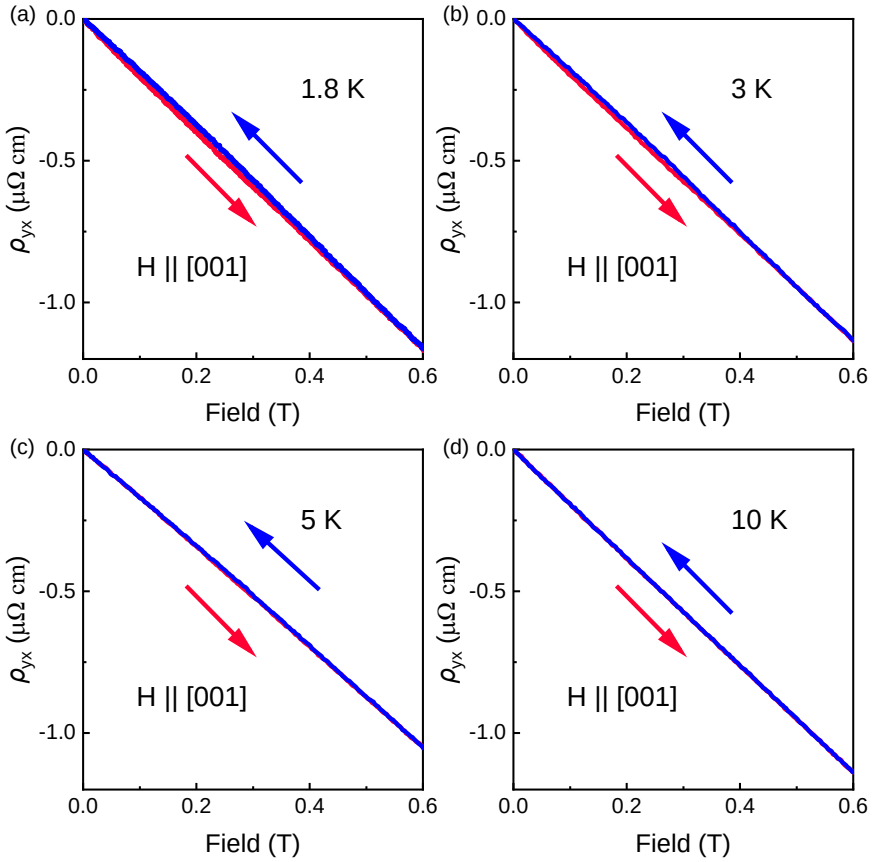

FIG. S1. (a - d) The Hall resistivity measured with magnetic along the [001] direction at 1.8K, 3K, 5K and 10K, respectively. The unusual Loop Hall Effect (LHE) is observed, and the LHE is suppressed with the temperature increasing. The Loop Hall effect is related to the relative positions of the Weyl point and the Fermi levels for CeAlSi.